

SIMULATION OF AN UNDERWATER HEXAPOD ROBOT

C. Georgiades¹, M. Buehler² and M. Nahon¹

¹Center for Intelligent Machines, McGill University, Montreal, Canada

christina.georgiades@mail.mcgill.ca, meyer.nahon@mcgill.ca

²Boston Dynamics Inc., Boston

buehler@bostondynamics.com

Abstract

AQUA is an underwater hexapod robot that uses its paddles to propel itself and control its orientation. To aid in the vehicle development, a simulation was needed to predict the motion of the robot based on its paddle oscillations. The most difficult aspect of this simulation was the characterization of the forces generated by the paddles oscillating in the water. In this work, a model predicting the forces produced by an oscillating rigid paddle was developed and validated experimentally. Tests were performed on an experimental setup, which was designed and built to measure the forces and torques produced by a paddle oscillating in a water tank. Also, the forces produced by a flexible fin were determined experimentally and were compared to those generated by the rigid paddle. Finally, a simulation of the AQUA robot was developed, based on the validated rigid paddle model.

1. Introduction

AQUA is an underwater robot based on RHex, a terrestrial six-legged robot developed in a collaboration between the Ambulatory Robotics Laboratory at McGill University, the University of Michigan, the University of California at Berkeley and Carnegie Mellon University, with sponsorship from DARPA [1]. RHex is a power autonomous robot with compliant recirculating semicircular legs, each with a single actuator. Three amphibious robots were successively designed, based on RHex: Shelley-RHex, Rugged-RHex and AQUA [2]. AQUA, shown in Figure 1, is a power autonomous tethered robot, which can walk on land using semicircular legs, or swim underwater using flexible paddles. The oscillating flexible paddles propel the robot and act as surfaces for orientation control. AQUA can be deployed from the beach, operate in shallow water, crawl on the ocean bottom and swim underwater.

There exist many other underwater robots, and these can be classified into Autonomous Underwater Vehicles (AUVs), Remotely-Operated Underwater Vehicles (ROVs), and bottom-crawling legged underwater robots. While legged underwater robots can crawl on land and on the ocean bottom, they cannot navigate the water column above the ocean bottom.

Conversely, thruster-based AUVs and ROVs can roam in that water column, but cannot be deployed from the beach, nor can they be operated in shallow water. Another key difference between AQUA and thruster-based aquatic vehicles is that AQUA uses paddles instead of thrusters and control surfaces to achieve propulsion and orientation control.

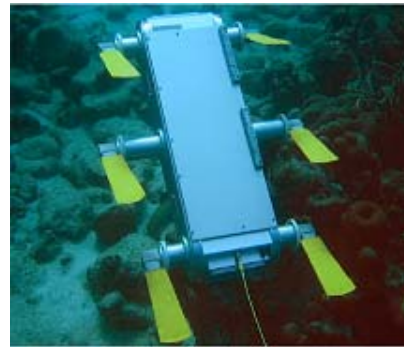


Figure 1: The AQUA Underwater Robot

Other robots have also made use of paddles or oscillating foils for propulsion and orientation control. In the mid-1990s, oscillating foils were proposed as an alternative to the conventional screw propeller to propel underwater vehicles [3],[4]. The idea that AUVs might propel themselves by flapping their tails like fish was popularized by MIT's Robotuna: an 8-link, foil-flapping robotic mechanism [5].

More recently, there has been growing interest in the design and control of underwater robots that propel themselves and maneuver with fins. PilotFish is a vehicle with four actuated single-degree-of-freedom foils aimed at demonstrating the capabilities of Nekton's oscillating fin thrusters [6]. Fish et al. discuss the conceptual design of a biomimetic AUV using two sets of four fins, each having two actuated degrees of freedom [7]. Licht et al. discuss a biomimetic flapping foil AUV with four oscillating foils, each with two actuated degrees of freedom [8].

A number of researchers have developed analytical models for the forces generated by oscillating foils. Harper et al. presented a model for oscillating-foil propulsion in which springs are used to transmit forces

from the actuators to the foils [9]. Kelly et al. proposed a model for planar carangiform (tuna-like) swimming based on reduced Euler-Lagrange equations for the interaction of a rigid body and an incompressible fluid [10]. Mason et al. built a three-link robot system to study carangiform-like swimming [11] and experimentally verified a quasi-steady fluid flow model to predict the thrust generated by a flapping tail.

Triantafyllou et al. carried out a review of the experimental work done in biomimetic foils [12]. Steadily oscillating two-dimensional foils were found to exhibit reverse Karman streets. Sparenberg and Wiersma [13], and Beal et al. [14] and others have investigated the interaction of foils with upstream vorticity. In some cases, interactions resulted in substantial increase of efficiency or increase of thrust at the expense of reduced efficiency. When two or more foils operate side by side, or near a wall or vehicle, interaction effects may result in a drag wake and deterioration of performance.

Computational Fluid Dynamics (CFD) analysis has also been used to characterize the forces generated by oscillating fins, as exemplified by the works of Ramamurti and Sandberg [15] and Singh et al. [16]. However, accurate computational modeling of flows in complex bio-hydrodynamic configurations remains a challenging problem.

Also relevant is experimental work on fin shape, aspect ratio and flexibility. Kemp et al. [17] report experiments with a low-aspect ratio pitching foil, whose propulsive efficiency doubles when the flexibility of the fin is optimized. Prempraneerach et al. [18] show that chord-wise flexibility can have a significant effect on the propulsive efficiency of two-dimensional heaving and pitching foils.

AQUA has six flexible paddles, each having one actuated degree of freedom. In simulating the vehicle, the most difficult aspect was the characterization of the forces generated by the paddles oscillating in the water. The models of [9], [10] and [11] were found to be too complex to adapt to our simulation. Instead, a model for rigid paddles was developed based on work done by Healey et al. [19]. The model was validated experimentally and incorporated into a simulation of the AQUA robot.

2. Rigid Paddle Model

The model for the rigid paddle was based on work done by Healey et al. [19] on the four quadrant dynamic response of conventional AUV thrusters. That model allows a calculation of the blade lift and drag forces for angles of attack ranging between 0° and 360° . The lift and drag coefficients vs. angle of attack from that model are shown in Figure 2.

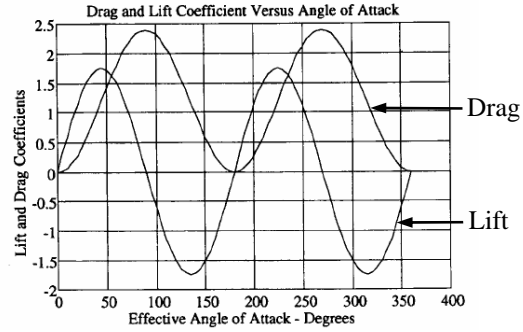


Figure 2: Lift and drag coefficients vs. angle of attack [19].

In our rigid paddle model, the scenario of a paddle of length l and width w moving with respect to an inertial frame is considered. Figure 3 illustrates the paddle and the inertial frame XYZ . The paddle, shown from its side, has a width w into the page and the inertial frame has its y -axis coming out of the page. The paddle is hinged at the origin of the inertial frame and rotates in the XZ plane about its shorter edge, which is aligned with the Y -axis of the inertial frame. The possibility of the fluid having a velocity with respect to the inertial frame is also considered. That velocity will hereafter be called inflow velocity.

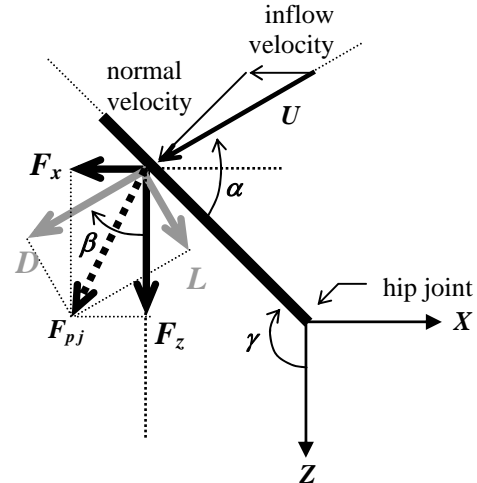


Figure 3: Rigid paddle and inertial frame XYZ .

The normal velocity, shown in Figure 3, is due to the paddle motion and is perpendicular to the paddle. It is equal in magnitude and opposite in direction to the velocity of the point on the paddle where lift and drag forces are applied. The flow impinging on the paddle with velocity U is a vector sum of inflow and normal velocities, as shown in Figure 3.

The angle β represents the direction of flow impinging on the paddle, relative to the Z -axis, while the angle γ represents the angular position of the paddle relative to

that axis. Angles β and γ are both positive counter clockwise, and so both those angles shown in Figure 3 are negative. The angle of attack α is the direction of flow relative to the paddle and can be calculated as $\alpha = \beta - \gamma$.

A paddle moving through a fluid generates drag and lift forces. As shown in Figure 3, the lift force L is perpendicular to the flow impinging on the paddle, while the drag force D is in line with that flow. Lift and drag forces vary as follows [19]:

$$L = 0.5 \rho U^2 S C_{L_{\max}} \sin(2\alpha) \quad (1)$$

$$D = 0.5 \rho U^2 S C_{D_{\max}} (1 - \cos(2\alpha)) \quad (2)$$

where ρ is the density of water, S is the planform area of the paddle, α is the angle of attack and U is the velocity of the flow impinging on the paddle. $C_{L_{\max}}$ and $C_{D_{\max}}$ are the maximum lift and drag coefficients of the paddle. Lift and drag forces can be transformed into the inertial frame of reference, using

$$F_x = D \sin \beta + L \cos \beta \quad (3)$$

$$F_z = -L \sin \beta + D \cos \beta \quad (4)$$

2.1. Rigid Paddle Oscillations

The model presented in Section 2 predicts forces generated by the paddle at any instant in time given the paddle trajectory (γ and $\dot{\gamma}$) and the inflow velocity. The paddle trajectory is periodic and each cycle consists of two phases: stroke and recovery. During stroke, the paddle sweeps a given angle in one direction. During recovery, the paddle sweeps the same angle in the opposite direction. In the present work, a cubic spline is used to generate this trajectory, as it can describe an asymmetric motion in which the stroke and recovery phases are of different durations. The trajectory is characterized by four parameters: the amplitude of oscillation A which refers to the angle swept by the paddle (Figure 4), the offset angle γ_0 about which the motion is centered (Figure 4), the period of oscillation T which is the time taken to complete one cycle, and the oscillation ratio R , which is defined as the ratio of the duration of the stroke to the duration of the entire oscillation (stroke and recovery). These parameters are used to generate the detailed time history of the paddle trajectory [20].

2.2. Estimation of inflow

A paddle performing a symmetric oscillation in a fluid with zero inflow velocity produces no thrust. However, as will be shown in this section, the same oscillation in a fluid with non-zero inflow velocity does produce useful thrust. Even if the paddle's hinge axis is

stationary with respect to the surrounding fluid, the paddle entrains water during oscillation, thus creating an inflow. In order to compare stagnant tank test results with rigid paddle simulations, inflow had to be quantified. Since inflow was not measured during the experiments, a method to estimate it had to be devised.

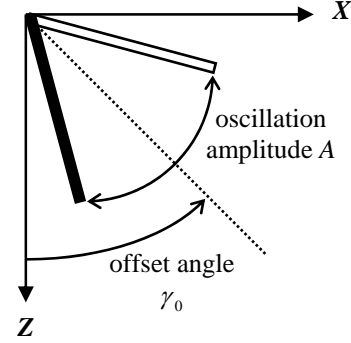


Figure 4: Oscillation amplitude A and angle γ_0

The inflow estimate is based on the premise that the water in front of the oscillating paddle moves to replace the volume of water displaced by the paddle. The rate at which the volume of water is displaced by the paddle during sweep or recovery corresponds to the rate at which water flows towards the paddle through a cross-section equal to half the frontal area of the volume swept by the paddle, as shown in Figure 5:

$$\frac{V_d}{T/2} = A_f v \quad (5)$$

where V_d is the displaced water volume, $T/2$ is half the period of oscillation, A_f is the frontal area of the paddle and v is the inflow velocity. The displaced volume V_d and the frontal area A_f can be obtained by geometry using Figure 5. Replacing the displaced volume V_d and the frontal area A_f in equation (5) by expressions derived from Figure 5, allows an estimation of v :

$$v = \frac{l A}{T \sin\left(\frac{A}{2}\right)} \quad (6)$$

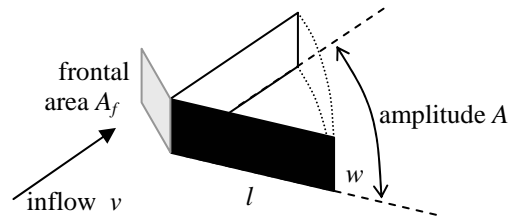


Figure 5: Diagram showing the volume swept by paddle and the frontal area of the paddle.

The variation of inflow velocity with A and T is shown in Figure 6. The inflow is inversely proportional to period and only weakly dependent on amplitude.

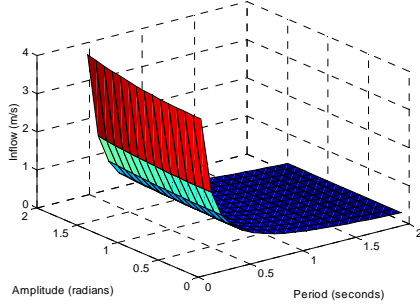


Figure 6: Inflow estimate as function of period and amplitude of oscillation for $l = 0.20\text{m}$, $w=0.05\text{ m}$

Figure 7 shows the lift and drag forces generated by a paddle of dimension $l = 0.2\text{m}$, $w = 0.05\text{m}$, with $C_{L\text{max}} = 0.92$ and $C_{D\text{max}} = 1.12$, following a symmetric trajectory for which $A = 90^\circ$, $T = 1\text{s}$ and $\gamma_0 = 0^\circ$ in the presence of inflow. The corresponding instantaneous parallel and perpendicular forces are shown in Figure 8. The parallel and perpendicular impulses, which are the integrals of the forces over time, are also shown in Figure 8. It can be seen in Figure 8 that the parallel impulse at the end of each oscillation increases steadily while the perpendicular impulse is equal to zero. Practically, this means that, in the presence of inflow, there is a net thrust but no net side force.

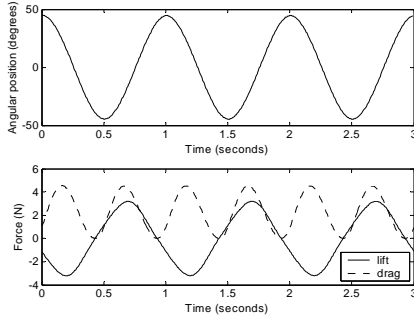


Figure 7: Lift and drag generated during a symmetric trajectory with inflow of 0.44m/s .

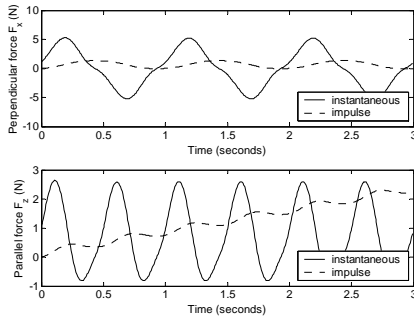


Figure 8: Parallel and perpendicular forces generated during a symmetric trajectory with inflow of 0.44m/s .

3. Thrust Measuring Setup

The Thrust Measuring Setup (TMS) is an experimental facility for the measurement of forces and torques generated by an oscillating paddle. The TMS was designed to allow validation of the rigid paddle model presented in Section 2 and to support later development of models for flexible fins.

The experiments were conducted in a stagnant water tank having a length of 6m , a width of 1.5m and a depth of 1.2m . An instrumented leg unit was positioned centrally along the width of the tank, 2m from one end of the tank, with the paddle oscillating in a plane 0.15m below the water surface. The tank was considered to be large enough that effects such as turbulence, recirculation and slosh would not affect experimental measurements.

The leg unit consists of the paddle under test, the motor assembly (motor, gearhead and encoder) and the six-axis force/torque sensor. The sensor is mounted between the support structure and the motor assembly. The motor assembly is enclosed in a cylindrical casing with a motor shaft extension protruding from the bottom to which the paddle under test is attached.

The setup was attached to the tank's two central vertical beams using a single brace across the width of the tank. High frequency noise was present in the data due to vibrations of the test structure [20]. The natural frequencies of the setup were measured from impact tests on the structure and dominant natural frequencies of 16 Hz and 48 Hz were found. Noise at these two distinct frequencies, as well as high frequency noise from the force/torque sensor, was present in the force/torque measurements of all experiments. A double-pass third-order Butterworth filter with a break frequency of 7 Hz was applied to all force and torque measurements in order to attenuate this noise.

The control electronics of the TMS include a National Instruments data acquisition card and breakout box, an amplifier, a filter card, 48V and 5V DC power supplies and a quadrature encoder decoder.

The acquisition of the experimental data and the control of the paddle were both executed at 100 Hz using a LabVIEW program. By connecting block diagrams of the virtual instrument (VI) libraries that come with LabVIEW as well as those supplied with the ATI Force/Torque sensor, a graphical user interface (GUI) was constructed. Pull-down menus allow the user to select test parameters prior to the start of an experiment and to display real time test information during the experiment.

When starting an experiment, the program first calibrates the paddle position relative to the

force/torque sensor coordinate frame. Then, the paddle follows the user-prescribed trajectory for a length of time or number of cycles. A PD controller sends torque commands to the paddle motor, based on the errors in the paddle's angular position and angular velocity. The desired paddle angular position and velocity are generated from the user-specified cubic spline trajectory. The control gains were tuned to obtain the best possible tracking of the desired trajectory.

4. Thrust Measuring Experiments

Experiments were performed on the thrust measuring setup with a rigid paddle in order to validate the model presented in Section 2. This section summarizes the results of those tests and compares them to those of the rigid paddle model. As well, the forces generated by a flexible fin are compared to those produced by the rigid paddle.

4.1. Rigid Paddle and Flexible Fin Experiments

The rigid paddle was oscillated at four different periods (0.4 seconds, 0.6 seconds, 0.8 seconds and 1 second) and eight different amplitudes (20° to 90° in increments of 10°) for each period.

The time histories of the parallel and perpendicular experimental forces were integrated, and then divided by the length of the experiments to calculate time-averaged parallel and perpendicular forces. Results showed that paddle oscillations of shorter periods and larger amplitudes produce larger parallel time-averaged forces. These results can be seen in Figure 9 and Figure 10, which also show the time-averaged simulated forces. The figures demonstrate a good match between the experimental and simulated results, indicating that the inflow velocity was estimated correctly in the simulations.

The power required to drive the paddle was evaluated by calculating the product of torque and paddle angular velocity. Although oscillations of smaller periods generate a greater time-averaged parallel force than do oscillations of larger periods with equal amplitude, they require greater average power. Because oscillations producing a greater parallel force require greater power to do so, it is important to examine the ratio of parallel force to power required as a measure of paddling efficiency. These power-normalized thrust results [20] do not vary greatly for different oscillations, but appear to show that longer periods produce greater power-normalized thrust.

Tests were also performed with different flexible fins [20]. For all experiments, the flexible fin produced more net thrust than did the rigid paddle. For example, a flexible fin oscillating with a period of 0.6 seconds and an amplitude of 37° produced time-averaged

parallel and perpendicular forces of 0.70N and -0.08 N respectively, while a rigid paddle undergoing the same motion generated forces of 0.21N and -0.04 N respectively. The thrust force produced by the flexible fin was 3.3 times greater than the thrust force produced by the rigid paddle. The side force produced by the flexible fin was twice that produced by the paddle, but both forces were negligible in magnitude.

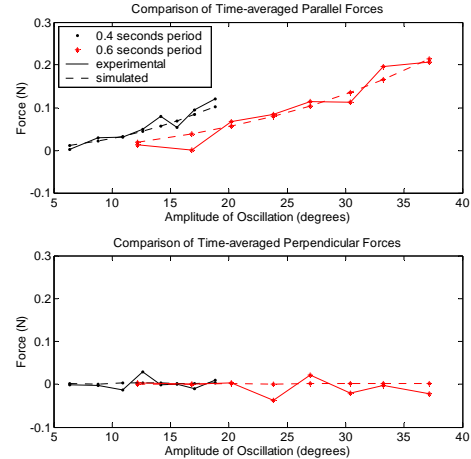


Figure 9: Comparison between experimental and simulated results for oscillations with periods of 0.4s and 0.6s.

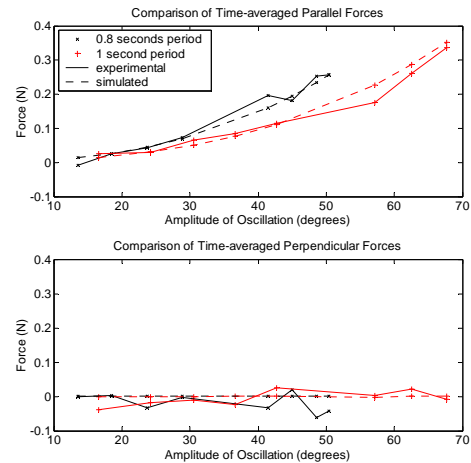


Figure 10: Comparison between experimental and simulated results for oscillations with periods of 0.8s and 1s.

Although the flexible fin is capable of producing greater forces, it requires more power to do so. Dividing the time-averaged forces by the average power required to perform the oscillations resulted in power-normalized time-averaged parallel and perpendicular forces of 0.60N/W and -0.07 N/W for the flexible fin and 0.49N/W and -0.05 N/W for the rigid

paddle. It is interesting to note that the flexible fin produces only 1.2 times more thrust than does the rigid paddle for a given amount of power. Thus, the flexible fin has the main advantage of generating greater thrust than does the rigid paddle, but it does so only slightly more efficiently than the rigid paddle.

Videos of sea turtles provided inspiration to develop a gait mimicking their paddle motion, in which the stroke is faster than the recovery. In simulations, a rigid paddle sweeping 180° rapidly in one direction and returning slowly to the starting position generated large net thrust while still producing near zero side force. Experiments verified this. The flexible fin was oscillated with an amplitude of 130° , a period of 1 second and oscillation ratios R of 0.2 to 0.5. Results showed that smaller oscillation ratios result in greater parallel time-averaged forces [20]. In terms of efficiency, oscillation ratios of 0.3 to 0.5 all yielded similar values of power-normalized forces, but at $R = 0.2$, that value was 30% higher, indicating greater efficiency. In general, asymmetric strokes appear to promise an advantage in producing more thrust, but at the cost of proportionally more power. For example, with $R = 0.2$, the most efficient oscillation, time-averaged parallel and perpendicular forces were 2.39N and -0.14N, while the corresponding power-normalized forces were 0.44 N/W and -0.03 N/W.

5. Equations of Motion

In developing the AQUA vehicle model, it was assumed that the underwater vehicle is moving in a stationary body of water having constant properties. The neutrally buoyant vehicle is approximated as a rigid rectangular prism of length 0.66m, width 0.22m and height 0.13m having a constant mass of 18 kg. Attached to the body is the coordinate frame xyz , which has its origin at the center of mass of the body, its x -axis pointing forward, its y -axis out the right side and its z -axis pointing downward, as shown in Figure 11. In the simulation, the robot moves with respect to an inertial frame XYZ .

The robot has six degrees of freedom: surge, sway, heave, roll, pitch and yaw, as shown in Figure 11. The translational motions (surge, sway and heave) obey Newton's law and the rotational motions (roll, pitch and yaw) are governed by Euler's equation. Fossen derived the rigid-body dynamics of a marine vehicle [21], and expressed the 6 DOF nonlinear dynamic equations of motion as:

$$\vec{F} = \mathbf{M} \dot{\vec{v}} + \mathbf{C}(\vec{v}) \vec{v} \quad (7)$$

where \vec{F} is a vector of forces and moments acting on the rigid body, \mathbf{M} is the inertia matrix, $\mathbf{C}(\vec{v})$ is the matrix of Coriolis and centripetal terms and \vec{v} is the

robot's generalized velocity vector $\vec{v} = [\vec{v}_{cm}^T \ \vec{\omega}^T]^T$

where $\vec{v}_{cm} = [u \ v \ w]^T$ is the velocity of the center of mass, $\vec{\omega} = [p \ q \ r]^T$ is the angular velocity vector with components p , q and r when expressed in the body frame.

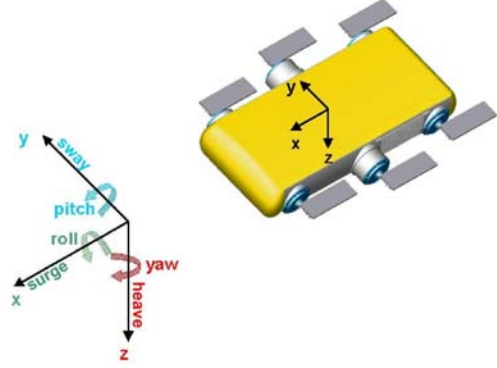


Figure 11: robot-fixed coordinate frame xyz and six degrees of freedom of AQUA.

When a body is accelerated in water, the fluid surrounding it is also accelerated. The concept of added mass represents the effect of fluid being accelerated by the body. The added mass forces and moments are contained in an added inertia matrix \mathbf{M}_A and a matrix of added hydrodynamic Coriolis and centripetal terms $\mathbf{C}_A(\vec{v})$. Matrix \mathbf{M} in equation (7) is equal to $\mathbf{M}_{RB} + \mathbf{M}_A$, where \mathbf{M}_{RB} is the rigid-body inertia matrix and \mathbf{M}_A is the added inertia matrix. Matrix $\mathbf{C}(\vec{v})$ is equal to $\mathbf{C}_{RB}(\vec{v}) + \mathbf{C}_A(\vec{v})$, where $\mathbf{C}_{RB}(\vec{v})$ is the rigid-body Coriolis and centripetal matrix and $\mathbf{C}_A(\vec{v})$ is the matrix of added hydrodynamic Coriolis and centripetal terms.

For symmetric slender bodies, only the diagonal terms of \mathbf{M}_A need be considered, namely the added mass hydrodynamic derivatives, $X_{\dot{u}}$, $Y_{\dot{v}}$, $Z_{\dot{w}}$, $L_{\dot{p}}$, $M_{\dot{q}}$ and $N_{\dot{r}}$, which appear in \mathbf{M}_A and $\mathbf{C}_A(\vec{v})$. They can be obtained by applying strip theory [21] in which the submerged vehicle is divided into a number of strips. Two-dimensional added mass hydrodynamic derivatives are computed for each strip and integrated over the third dimension. AQUA's six added mass hydrodynamic derivatives were estimated using that principle and found to be [20] $X_{\dot{u}}=6.98\text{kg}$, $Y_{\dot{v}}=14.50\text{kg}$, $Z_{\dot{w}}=32.41\text{kg}$, $L_{\dot{p}}=0.40\text{kg}\cdot\text{m}^2$, $M_{\dot{q}}=1.19\text{kg}\cdot\text{m}^2$ and $N_{\dot{r}}=0.55\text{kg}\cdot\text{m}^2$.

Equation (7) can be expanded to obtain the following six non-linear, coupled differential equations of motion:

$$F_{cmx} = m(\dot{u} - vr + wq) - X_{\dot{u}}\dot{u} - Z_{\dot{w}}wq + Y_{\dot{v}}vr \quad (8)$$

$$F_{cm y} = m(\dot{v} - wp + ur) - Y_{\dot{v}}\dot{v} + Z_{\dot{w}}wp - X_{\dot{u}}ur \quad (9)$$

$$F_{cmz} = m(\dot{w} - uq + vp) - Z_{\dot{w}}\dot{w} - Y_{\dot{v}}vp + X_{\dot{u}}uq \quad (10)$$

$$\begin{aligned} M_{cmx} = & I_{xx}\dot{p} + (I_{zz} - I_{yy})qr - (\dot{r} + pq)I_{xz} \\ & + (r^2 - q^2)I_{yz} + (pr - \dot{q})I_{xy} - L_{\dot{p}}\dot{p} \\ & + (Y_{\dot{v}} - Z_{\dot{w}})vw + (M_{\dot{q}} - N_{\dot{r}})qr \end{aligned} \quad (11)$$

$$\begin{aligned} M_{cm y} = & I_{yy}\dot{q} + (I_{xx} - I_{zz})rp - (\dot{p} + qr)I_{xy} \\ & + (p^2 - r^2)I_{xz} + (qp - \dot{r})I_{yz} - M_{\dot{q}}\dot{q} \\ & + (Z_{\dot{w}} - X_{\dot{u}})uw + (N_{\dot{r}} - L_{\dot{p}})pr \end{aligned} \quad (12)$$

$$\begin{aligned} M_{cmz} = & I_{zz}\dot{r} + (I_{yy} - I_{xx})pq - (\dot{q} + rp)I_{yz} \\ & + (q^2 - p^2)I_{xy} + (rq - \dot{p})I_{xz} - N_{\dot{r}}\dot{r} \\ & + (X_{\dot{u}} - Y_{\dot{v}})uv + (L_{\dot{p}} - M_{\dot{q}})pq \end{aligned} \quad (13)$$

where F_{cmx} , $F_{cm y}$ and F_{cmz} are body-frame components of \vec{F}_{cm} , the total external force acting on the robot, while M_{cmx} , $M_{cm y}$ and M_{cmz} are body-frame components of \vec{M}_{cm} , the total external moment acting at the center of mass of the robot.

5.1. Calculation of Forces and Moments

The force \vec{F}_{cm} and moment \vec{M}_{cm} of equations (8) to (13) are generated by gravitational, buoyancy, hydrodynamic and propulsive effects:

$$\vec{F}_{cm} = \vec{F}_g + \vec{B} + \vec{F}_p + \vec{F}_h \quad (14)$$

$$\vec{M}_{cm} = \vec{M}_b + \vec{M}_p + \vec{M}_h \quad (15)$$

where \vec{F}_g is the gravitational force, \vec{B} is the buoyancy force, \vec{F}_p is the propulsive force and \vec{F}_h is the hydrodynamic force. Similarly, \vec{M}_b is the buoyancy moment, \vec{M}_p is the propulsive moment and \vec{M}_h is the hydrodynamic moment.

5.1.1. Gravitational and Buoyancy Forces

The gravitational force \vec{F}_g acts through the center of mass of the robot and is directed in the positive direction of the Z-axis of the inertial frame. It is equal to $m\vec{g}$, where m is the mass of the robot and \vec{g} is the gravitational acceleration. The buoyancy force \vec{B} passes through the volumetric center of the robot and acts in the negative Z-direction of the inertial frame. It

is equal to the weight of the water displaced by the robot. These forces can be transformed into the body frame to yield

$$\vec{F}_g + \vec{B} = \begin{bmatrix} F_{gx} \\ F_{gy} \\ F_{gz} \end{bmatrix} + \begin{bmatrix} B_x \\ B_y \\ B_z \end{bmatrix} = (mg - \rho Vg) \begin{bmatrix} -\sin \theta \\ \sin \phi \cos \theta \\ \cos \phi \cos \theta \end{bmatrix} \quad (16)$$

where ϕ , θ and ψ are the roll, pitch and yaw angles defined by standard aeronautical convention [22]. Since the gravitational force acts through the center of mass, it produces no moment about the center of mass. The buoyancy moment \vec{M}_b is the cross product between the position vector of the center of buoyancy with respect to the center of mass, and the buoyancy force:

$$\vec{M}_b = \begin{bmatrix} M_{bx} \\ M_{by} \\ M_{bz} \end{bmatrix} = \rho Vg \begin{bmatrix} -y_b(\cos \phi \cos \theta) + z_b(\sin \phi \cos \theta) \\ x_b(\cos \phi \cos \theta) + z_b(\sin \theta) \\ -x_b(\sin \phi \cos \theta) - y_b(\sin \theta) \end{bmatrix} \quad (17)$$

where x_b , y_b and z_b are the body-frame components of the vector from the center of mass to the center of buoyancy. If the center of mass coincides with the volumetric center of the robot, x_b , y_b and z_b are zero and the buoyancy moment is null. In the simulation, this was assumed to be the case.

5.1.2. Hydrodynamic Force and Moment

The hydrodynamic force \vec{F}_h is a function of the vehicle motion and its geometry. The drag force on the body of the robot is taken to be the vector sum of the drag forces acting on the three faces of the parallelepiped exposed to the incoming flow. If the robot has velocities u , v and w along the x -, y - and z -axes, each relative flow velocity component causes a drag force on the exposed face of the prism to which it is perpendicular. The drag force on each of the three faces is $0.5\rho C_{Di}A_i v_i^2$, where $i = x, y$ or z and, C_{Di} is the drag coefficient of the corresponding face, A_i is the area of the face and v_i is the relative flow velocity component perpendicular to the face.

Coefficients C_{Dx} , C_{Dy} and C_{Dz} are the drag coefficients of the front, the right and the top faces of the robot. They were found from a set of data for sharp-edged rectangular prisms having the free stream normal to one face [23]. These relations are valid for a free-stream Reynolds number between 10^4 and 10^6 . In the simulation of AQUA, the Reynolds number is approximately 1.5×10^4 at a vehicle speed of 0.2m/s. A prism having AQUA's dimensions has C_{Dx} , C_{Dy} and C_{Dz} equal to 0.90, 1.08 and 1.22 respectively.

The drag forces along the x -, y - and z -axes are F_{hx} , F_{hy} and F_{hz} respectively. The hydrodynamic force vector acting on the robot is equal to:

$$\vec{F}_h = \begin{bmatrix} F_{hx} \\ F_{hy} \\ F_{hz} \end{bmatrix} = \begin{bmatrix} 0.5\rho C_{Dx}BH u^2 \\ 0.5\rho C_{Dy}LH v^2 \\ 0.5\rho C_{Dz}BL w^2 \end{bmatrix} \quad (18)$$

where B , H and L are the width, the height and the length of the robot.

The robot's angular velocity causes each point of the robot to have a velocity $\vec{v} = \vec{\omega} \times \vec{r}$, where $\vec{r} = [x \ y \ z]^T$ is the position of the point with respect to the center of mass. For a given $\vec{\omega}$, the velocity of each point of the robot was calculated, and the corresponding drag force was calculated at each point. The drag forces have a magnitude proportional to \vec{v}^2 and a direction opposite to \vec{v} . Although the drag forces on opposing faces cancel each other out, they create a drag moment \vec{M}_h about the center of mass, hereafter called hydrodynamic moment. The hydrodynamic moments M_{hx} , M_{hy} and M_{hz} represent the robot's resistance to rotation about the x -, y - and z -axes respectively, and are given by [20]:

$$\vec{M}_h = \begin{bmatrix} M_{hx} \\ M_{hy} \\ M_{hz} \end{bmatrix} = \begin{bmatrix} \rho p^2 L (C_{Dz} B^4 + C_{Dy} H^4) \\ \frac{64}{\rho q^2 B (C_{Dx} H^4 + C_{Dz} L^4)} \\ \frac{64}{\rho r^2 H (C_{Dx} B^4 + C_{Dy} L^4)} \end{bmatrix} \quad (19)$$

5.1.3. Propulsive Force and Moment

The propulsive force \vec{F}_p of the robot comes from the movement of its paddles, which are modeled as flat plates, as explained in Section 2 with one important difference. Whereas, in Section 2, the inflow velocity estimated was due to the water entrained by the paddle, in the simulation of the robot, the inflow at each hip is taken to be the opposite of the velocity of that hip through the water. As a result, the j -th paddle force can be written as:

$$\vec{F}_{p_j} = \begin{bmatrix} F_{px_j} \\ F_{py_j} \\ F_{pz_j} \end{bmatrix} = \begin{bmatrix} D_j \sin \beta_j + L_j \cos \beta_j \\ 0 \\ -L_j \sin \beta_j + D_j \cos \beta_j \end{bmatrix} \quad (20)$$

where D_j and L_j are the drag and lift forces produced by paddle j and β_j is the angle, in the xyz coordinate frame of paddle j .

The propulsive force creates a moment \vec{M}_p , which acts on the center of mass. The propulsive moment due to the propulsive force acting at hip j is given by

$$\vec{M}_{p_j} = \begin{bmatrix} x_{hip_j} \\ y_{hip_j} \\ z_{hip_j} \end{bmatrix} \times \begin{bmatrix} F_{px_j} \\ F_{py_j} \\ F_{pz_j} \end{bmatrix} \quad (21)$$

$$= \begin{bmatrix} y_{hip_j} (-L_j \sin \beta_j + D_j \cos \beta_j) \\ -x_{hip_j} (-L_j \sin \beta_j + D_j \cos \beta_j) + z_{hip_j} (D_j \sin \beta_j + L_j \cos \beta_j) \\ -y_{hip_j} (D_j \sin \beta_j + L_j \cos \beta_j) \end{bmatrix}$$

where x_{hip_j} , y_{hip_j} and z_{hip_j} give the position of hip j with respect to the center of mass in the coordinate frame fixed to the robot.

The total propulsive force for the vehicle is the sum of the six propulsive forces given by equation (20). The total propulsive moment at the center of mass about the x -, y - and z -axes is the sum of the moments generated by the six propulsive forces given by equation (21).

5.2. Numerical Simulation

The gravity, buoyancy, hydrodynamic and propulsive force and moment expressions are substituted into equations (8) to (13), which can then be put in the form $\dot{\vec{x}} = f(\vec{x}, \vec{u})$ where $\vec{x} = [u \ v \ w \ p \ q \ r \ \phi \ \theta \ \psi]^T$ represents the state of the system and \vec{u} is a vector of inputs characterizing the paddle motion. Based on the initial state \vec{x}_0 and the time-varying input \vec{u} , the goal is to find the resulting state \vec{x} . The simulation inputs are the variables characterizing the oscillation of the paddles: the amplitude and period of oscillation, the offset angle, and the oscillation ratio. The outputs of the simulation are the position and orientation of the robot in the inertial frame XYZ. In order to obtain \vec{x} , $\dot{\vec{x}}$ is calculated and integrated. The numerical integration is performed using Simulink®, a software package for modeling, simulating, and analyzing dynamical systems.

For an input where all paddles oscillate with a period of 0.7 seconds, an amplitude of 27° , an offset angle in line with the back of the robot and an oscillation ratio of 0.5, the robot, which has an initial velocity of 0m/s, traverses 2m in 21 seconds. It should be recalled from Section 4.1 that the flexible fin produced about 3 times more thrust than the flat plate for a given oscillation. To represent the use of flexible fins, the forces produced by the rigid paddle were multiplied by 3 in the simulation and the robot then traversed 6.7m in 21 seconds. As a point of comparison, pool tests were performed with the real vehicle with flexible fins in July 2004. For the same paddle motion, the real vehicle, which also had an initial velocity of 0m/s, traversed 6.4m in 21 seconds. Thus, the simulation of

the robot gives outputs that are consistent with those observed in the pool.

Figure 12 shows a more complex maneuver. All paddles of the robot except the middle right paddle oscillate with a period of 1 second, an amplitude of 6° , an offset angle in line with the back of the robot and the bottom of the robot, and an oscillation ratio of 0.5. The middle right paddle oscillates with a period of 1 second, an amplitude of 46° , an offset angle that is half way between the back of the robot and the bottom of the robot, and an oscillation ratio of 0.5. The robot pitches down, as it turns and rolls left. While doing that, the robot moves very little along the X-, Y- and Z-axes.

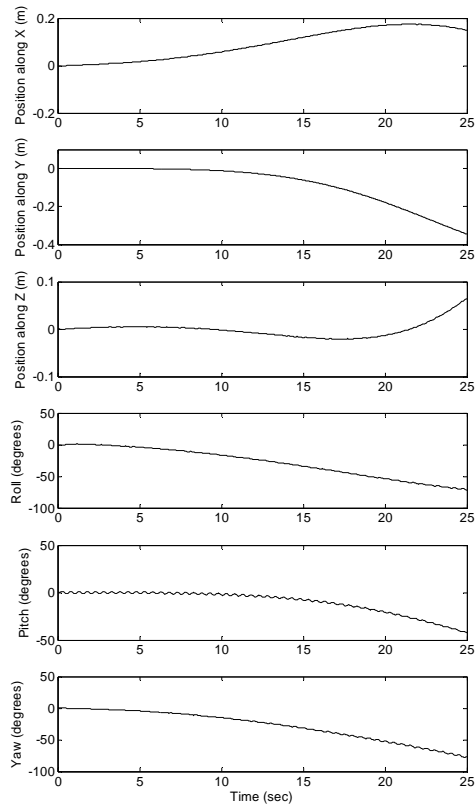


Figure 12: The robot position and orientation of the robot pitching down, as it turns and rolls left.

5.3. Animation

When many of state variables are nonzero, as in Figure 12, it can be difficult to visualize the motion of the robot in three dimensions. For that purpose, an animation of the motion of the robot was created. The robot position in the inertial frame, its orientation as well as the angular position of the paddles with respect to the robot were written to a file. A program was written in 3ds max®, a graphics and animation software, to read the file and produce an animation of

the motion of the robot. Figure 13 shows a few frames of an animation of the maneuver of Figure 12.

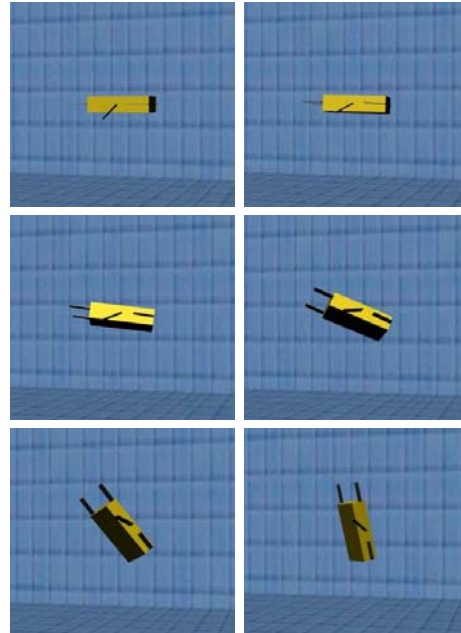


Figure 13: A few frames of an animation showing the robot pitching down, as it turns and rolls left.

6. Conclusions and Recommendations for Future Work

In this work, a model predicting the forces produced by an oscillating rigid paddle was developed. Rigid paddle and flexible fin experiments were performed on an experimental setup, which was designed and built to measure the forces and torques produced by a paddle oscillating in a water tank. The experimentally-measured forces were compared to those generated by the rigid paddle model. Finally, a simulation of the AQUA robot was developed, based on the validated rigid paddle model.

A number of improvements could be made to the model and to the experimental procedure. To avoid having to estimate the inflow, future experiments should include a flow sensor on the thrust measuring setup. Future tests in a tow tank would be useful to better understand the thruster effectiveness in a moving vehicle and to determine whether inflow related to water displacement should be incorporated in the simulation of the robot, particularly at low speeds. Tow tank tests would also allow determination of the validity of the drag model used for the body of the vehicle.

Acknowledgements

The authors gratefully acknowledge funding for this research from the Institute for Robotic and Intelligent Systems (IRIS).

References

- [1] U. Saranli, M. Buehler and D. E. Koditschek, "RHex: A Simple and Highly Mobile Hexapod Robot", *The International Journal of Robotics Research*, Vol. 20, pp. 616-631, 2001.
- [2] C. Prahacs, A. Saunders, M. K. Smith, D. McMordie and M. Buehler, "Towards Legged Amphibious Mobile Robotics", *The Inaugural Canadian Design Engineering Network (CDEN) Design Conference*, July 2004.
- [3] M. S. Triantafyllou and G. S. Triantafyllou, "An efficient swimming machine", *Scientific American*, March 1995.
- [4] J. Czarnowski, R. Cleary and B. Kremer, "Exploring the possibility of placing traditional marine vessels under oscillating foil propulsion.", *Proc. 7th Int. Offshore and Polar Engineering Conf.*, Vol. 2, pp. 76-81, May 1997.
- [5] D. Barrett, M. Grosenbaugh and M. Triantafyllou, "The optimal control of a flexible hull robotic undersea vehicle propelled by an oscillating foil", *Proc. IEEE Symp. Autonomous Underwater Vehicle Tech.*, 1996.
- [6] M. Kemp, B. Hobson, J. Janet, C. Pell and E. Tytell, "Assessing the Performance of Oscillating Fin Thruster Vehicles", *Proc. 12th Int. Symp. on Unmanned, Untethered Submersible Tech.*, 2001.
- [7] F. E. Fish, G. V. Lauder, R. Mittal, A. H. Techet, M. S. Triantafyllou, J. A. Walker and P. W. Webb, "Conceptual Design of the Construction of a Biorobotic AUV Based on Biological Hydrodynamics", *Proc. 13th Int. Symp. Unmanned Untethered Submersible Tech.*, pp. 207 – 209, 2003.
- [8] S. Licht, V. Polidoro, M. Flores, F. S. Hover and M. S. Triantafyllou, "Design and Projected Performance of a Flapping Foil AUV", *IEEE Journal of Oceanic Engineering*, Volume 29, Issue 3, pp. 786 – 794, 2004.
- [9] K. A. Harper, M. D. Berkemeier and S. Grace, "Modeling the dynamics of spring-driven oscillating-foil propulsion", *IEEE Journal of Oceanic Engineering*, Volume 23, pp. 285-296, 1998.
- [10] S. D. Kelly and R. M. Murray, "Modelling efficient pisciform swimming for control", *International Journal of Robust and Nonlinear Control*, Vol. 10, pp. 217-241, 2000.
- [11] R. Mason and J. W. Burdick, "Experiments in carangiform robotic fish locomotion", *Proc. IEEE Int. Conf. on Robotics and Automation*, Vol. 1, pp. 428 – 435, April 2000.
- [12] M. S. Triantafyllou, A. H. Techet, F. S. Hover, "Review of Experimental Work in Biomimetic Foils", *IEEE Journal of Oceanic Engineering*, Vol. 29, No. 3, pp. 585 – 594, 2004.
- [13] J. A. Sparenberg and A. K. Wiersma, "On the efficiency increasing interaction of thrust producing lifting surfaces", in *Swimming and Flying in Nature*, T. Wu, C. J. Brokaw and C. Brennen, Eds. New York: Plenum, Vol. 2, pp. 891–917, 1975.
- [14] D. N. Beal, F. S. Hover and M. S. Triantafyllou, "The effect on thrust and efficiency of an upstream Karman wake on an oscillating foil", *Proc. 12th Int. Symp. Unmanned Untethered Submersible Tech.*, 2001.
- [15] R. Ramamurti and W. C. Sandberg, "Simulation of flow about flapping airfoils using a finite element incompressible flow solver", *AIAA Journal*, Vol. 39, pp. 253-260, 2001.
- [16] S. N. Singh, A. Simha and R. Mittal, "Biorobotic AUV Maneuvering by Pectoral Fins: Inverse Control Design Based on CFD Parameterization", *IEEE Journal of Oceanic Engineering*, Vol. 29, No.3, 2004.
- [17] M. Kemp, B. Hobson and C. Pell, "Energetics of the oscillating fin thruster", *Proc. 13th Int. Symp. Unmanned Untethered Submersible Tech.*, 2003.
- [18] P. Prempraneerach, F. S. Hover and M. S. Triantafyllou, "The effect of chordwise flexibility on the thrust and efficiency of a flapping foil", *Proc. 13th Int. Symp. Unmanned Untethered Submersible Tech.*, 2003.
- [19] A. J. Healey, S. M. Rock, S. Cody, D. Miles and J. P. Brown, "Toward an Improved Understanding of Thruster Dynamics for Underwater Vehicles", *IEEE Journal of Oceanic Engineering*, Vol. 20, No. 4, pp. 354 – 361, 1995.
- [20] C. Georgiades, "Simulation and Control of an Underwater Hexapod Robot", M.Eng. Thesis, Dept. of Mechanical Engineering, McGill University, Montreal, Canada, 2005.
- [21] T. I. Fossen, *Guidance and Control of Ocean Vehicles*, John Wiley & Sons Ltd, UK, 1994.
- [22] B. Etkin, *Dynamics of Atmospheric Flight*, John Wiley & Sons Ltd, New York, 1972.
- [23] ESDU Fluid forces, pressures and moments on rectangular blocks. Engineering Sciences Data Item No. 71016, ESDU International plc., London, 1971.